J Mater Sci (2018) 53:15204–15212

Electronic materials

Metallized nanoporous anodic alumina films and their applications

G. A. Lyubas[1,*]

[1] Russian Academy of Sciences, Siberian Branch, Vorozhtsov Novosibirsk Institute of Organic Chemistry, pr. Lavrent'eva 9, Novosibirsk, Russia 630090

Received: 2 April 2018
Accepted: 10 July 2018
Published online: 16 July 2018

ABSTRACT

The optimal conditions of the aluminum electrochemical anodization and electrochemical and chemical metallization were determined. Metallized nanoporous anodic alumina (NAA) films with ultrahigh/average/low density of pores were obtained using the optimal conditions. The physical and chemical properties of the obtained NAA films were studied by high-resolution scanning electron microscopy and the reflective interference spectra in a wavelength range of 235–735 nm. Possible applications of the obtained NAA films are in micro/nanoscale lasers with indirect electrical pumping by laser diodes; optical interferometric chemical nanosensors; and the selective interference coloration and protection of the metal surface.

Introduction

Exploring the emerging trends in the realm of electrochemistry in particular the creation of nanoporous anodic alumina (NAA) is a topical problem of modern material engineering [1–33]. For example, NAA films with a high and average density of pores can be used in micro/nanoscale lasers with indirect electrical pumping by laser diodes [1]. Metallized NAA films with ultrahigh density of pores are preferable for optical interferometric chemical sensors [2]. Films with low density of pores are used in the selective interference coloration of the metal surface improving the corrosion resistance of the metal [3]. This work is a logical continuation of the works [1–3]. Determination of the optimal conditions of the aluminum electrochemical anodization and electrochemical and chemical metallization for each particular case is an important task. This work was aimed at obtaining in optimal conditions for the metallized NAA films with ultrahigh, average, and low density of pores and the study of their applications.

Experimental

Aluminum plates with a thickness of 0.1 mm, high-purity grade of 99.95% AL, and size of 50 × 50 mm^2 were used for anodization. Before anodizing, the plates were purified by degreasing in 10% solution of NaOH and blooming in 10% solution of nitric acid. Then, the material was electrochemically polished in a solution of the following composition: orthophosphoric acid (relative density of 1.7) 34 g, sulfuric acid

Address correspondence to E-mail: sciencenano@yandex.ru

https://doi.org/10.1007/s10853-018-2686-5

(relative density of 1.84) 34 g, chromic anhydride 4 g, and water to 100 g. The electropolishing mode was U_{post} = 12 V, temperature was 80–90 °C, and duration was 2–3 min. The anodization of the samples was carried out in 2 and 10% solutions of sulfuric (H_2SO_4), phosphoric (H_3PO_4) acids at U_{post} = 8–20 V (see Table 1). Deposition of copper (nickel) particles was performed electrochemically by the current of alternating polarity U_{alter} = 12–15 V from an electrolyte with the following composition: for Cu, copper sulfate 50 g/L, magnesium sulfate 20 g/L, and sulfuric acid (up to pH = 1); for Ni, nickel sulfate 40 g/L, cobalt sulfate 40 g/L and boric acid 40 g/L (see Table 2). Treatment time was 3–4 min. Further treatment of layers containing copper (nickel) nanoparticles in solutions of silver nitrate and gold tetrachloride to form silver and gold nanoparticles by exchange reactions was done from solutions of the following composition: for Ag, silver nitrate 1 g/L, sulfuric acid (to pH = 2); for Au, chloroauric acid ($HAuCl_4$) 1 g/L, sulfuric acid (see Table 2). Treatment time was 3–4 min.

The adsorption of rhodamine 6G molecules on NAA films in most cases was carried out from a solution with a concentration $C = 10^{-3}$ mol/L, which is the optimal value.

In order to obtain the images of pores with a superhigh resolution, we used a Zeiss MERLIN VP Compact scanning electron microscope with a resolution of 5 nm, which works at 20 kV.

In order to measure the laser-generation spectra, we used an Avantas (AvaSpec1024) spectrometer with a resolution of 0.4 nm in a wavelength range of 235–735 nm. In the pulsed mode, we used an Nd:YAG laser LOTIS TII (model LS2147) as a source of the laser-generation excitation in the samples. The measurements were carried out by single pulses on the second harmonic (wavelength λ_{ex} = 532 nm), pulse energy E from 0 to 90 mJ, and pulse duration t = 20 ns.

Reflective interference spectra (RIfS) of the studied NAA films were recorded on a AvaSpec1024 spectrometer at different incidence angles ranging from 10° to 85°. The light source was a halogen lamp (AvaLightDHS).

Results and discussion

Using of the above conditions and regimes of the aluminum electrochemical anodization and metallization the NAA films with ultrahigh density of pores, average density of pores, and low density of pores were obtained. The obtained metallized NAA films were studied by high-resolution scanning electron microscopy and RIfS.

Ultrahigh density of pores and high-sensitivity metallized NAA optical interferometric chemical sensors

Metallized NAA films with ultrahigh nanopore density were obtained. The electron microscopy image of the obtained metallized U-NAA-Cu-Ag film is shown in Fig. 1. Alumina film has ultrahigh density of pores at the minimum wall thickness. The

Table 1 The anodization parameters

Samples	Anodization time, min	Electrolyte	Voltage, V
Ultrahigh density of pores			
U-NAA-Cu-Ag	7 min 2% H_2SO_4 (U = 12 V) + 3 min 10% H_3PO_4 (U = 20 V)		
U-NAA-Ni-Ag	11 min 2% H_2SO_4 (U = 12 V) + 4 min 10% H_3PO_4 (U = 20 V)		
Average density of pores			
A-NAA-Cu-Ag	60	2% H_2SO_4	11
Low density of pores			
L-NAA	8	2% H_2SO_4	8
L-NAA-Cu	8		8
L-NAA-Cu-Ag	8		8
L-NAA-Cu-Au	8		8
Polarization anisotropy of reflection spectra and protection of documents			
P-NAA-Ni	15	2% H_2SO_4	12
B-NAA-Ni	{15 min 2% H_2SO_4 (U = 20 V) + 5 min 10% H_3PO_4 (U = 20 V)} × 6 repetitions		

Table 2 The conditions of the electrochemical and chemical metallization

Samples	Type of deposition	Voltage, V	Electrolyte
Ultrahigh density of pores			
U-NAA-Cu-Ag	Electrochemical (Cu)–chemical (Ag)	12–14	For Cu, copper sulfate 50 g/L, magnesium sulfate 20 g/L, and sulfuric acid (up to pH = 1); for Ag, silver nitrate 1 g/L, sulfuric acid (to pH = 2)
U-NAA-Ni-Ag	Electrochemical (Ni)–chemical (Ag)	12–15	For Ni, nickel sulfate 40 g/L, cobalt sulfate 40 g/L and boric acid 40 g/L; for Ag, silver nitrate 1 g/L, sulfuric acid (to pH = 2)
Average density of pores			
A-NAA-Cu-Ag	Electrochemical (Cu)–chemical (Ag)	12–14	For Cu, copper sulfate 50 g/L, magnesium sulfate 20 g/L, and sulfuric acid (up to pH = 1); for Ag, silver nitrate 1 g/L, sulfuric acid (to pH = 2)
Low density of pores			
L-NAA	–	–	–
L-NAA-Cu	Electrochemical (Cu)	12–14	Copper sulfate 50 g/L, magnesium sulfate 20 g/L, and sulfuric acid (up to pH = 1)
L-NAA-Cu-Ag	Electrochemical (Cu)–chemical (Ag)	12–14	For Cu, copper sulfate 50 g/L, magnesium sulfate 20 g/L, and sulfuric acid (up to pH = 1); for Ag, silver nitrate 1 g/L, sulfuric acid (to pH = 2)
L-NAA-Cu-Au	Electrochemical (Cu)–chemical (Au)	12–14	For Cu, copper sulfate 50 g/L, magnesium sulfate 20 g/L, and sulfuric acid (up to pH = 1); for Au, chloroauric acid ($HAuCl_4$) 1 g/L, sulfuric acid (to pH = 1–2)
Polarization anisotropy of reflection spectra and protection of documents			
P-NAA-Ni	Electrochemical (Ni)	12	Nickel sulfate 40 g/L, cobalt sulfate 40 g/L and boric acid 40 g/L
B-NAA-Ni	Electrochemical (Ni)	12	Nickel sulfate 40 g/L, cobalt sulfate 40 g/L and boric acid 40 g/L

pores are close to each other. The diameter of pores is about 14–25 nm. The porosity (P) is about 61%. The porosity can be calculated from Eq. (1) [32, 33]:

$$P = \frac{\pi}{2\sqrt{3}} \left(\frac{D}{L}\right)^2 \times 100\% = 90.7 \times \left(\frac{D}{L}\right)^2 \%, \quad (1)$$

where D is the pore diameter, L is the inter pore distance. The bright spheroid particles on the top of porous film are silver nanoparticles. The formed silver nanoparticles in porous films have a diameter from 12 to 25 nm and are located predominantly on the surface or near the upper boundary of the porous layer. Silver nanoparticles being reduced on copper inside the pores are released from the pores and localized on the surface. As can be seen from Fig. 1, silver nanoparticles are distributed on the surface of NAA at the distance of about 30–105 nm; i.e., the film is not continuous and pores are available for penetration of analyte molecules.

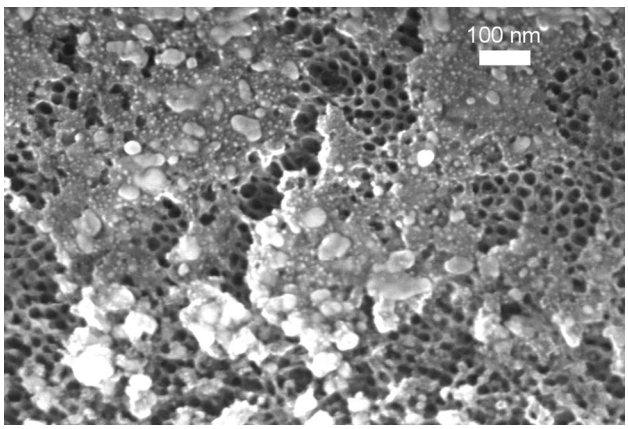

Figure 1 Scanning electron microscopic image of high resolution of metallized nanoporous layer of NAA with silver nanoparticles (top view; ultrahigh density of pores).

Possible applications of metallized NAA films with ultrahigh nanopore density are in optical interferometric chemical sensors. The porous nature of the NAA film allows it efficiently absorb the different solvents. The solvents absorption leads to changes in the RIfS. Upon filling NAA pores with the analyte, a change in the effective optical thickness (EOT = $2nl_{\text{eff}}$ [8]) of the sample takes place.

$$\text{EOT} = 2nl_{\text{eff}} = \frac{2n^2 l}{\sqrt{n^2 - \sin^2 \varphi}}, \quad (2)$$

where n is the index of refraction, l_{eff} is the effective thickness of the film, l is the thickness of the film, φ is

angle of incidence of light. The measured RIfS of the metallized U-NAA-Cu-Ag film covered by water and ethanol are shown in Fig. 2; entrance angle is 12°. In the absence of water, spectral maximum is located at ≈ 538 nm (see curve 1). In the presence of water, spectral maximum is shifted to the long-wave region on ≈ 29 nm (see curve 2). A similar shift in the RIfS is observed for ethanol (see curve 3). The organic solvent fills porous layer and increases the refractive index of NAA, so the wavelength of the reflection maximum is shifted to the long-wave spectral region. After solvent drying, the reflection maximum comes into initial position. The observed reversible spectral shift effect gives the possibility to create the simple high-sensitivity chemical sensors on the base of metallized NAA films. Figure 2 shows that, in the presence of ethanol, the spectral maximum is shifted to longer wavelengths by ≈ 47 nm (curve 3). The difference between the shifts of the maxima of water and ethanol is ≈ 18 ± 0.4 nm. The difference between refractive indices of water and ethanol is Δn = 0.028 (n_{water}= 1.333, $n_{ethanol}$= 1.361). Hence, we obtain the value of sensory sensitivity for the solvent equal to ≈ 643 nm/RIU, which is significantly more than the value obtained in [8], in which similar calculations for porous NAA give the value of 39 nm/RIU. The sensitivity for sensor systems based on the LSPR (localized surface Plasmon resonance) effect of single silver nanoparticles with the improved detection threshold to the change in the refractive index of the solvent is about ~ 200 nm/RIU [34], which is comparable with the sensitivity of the sensor on the effect of the RIfS shift obtained in the present study. Thus, the chemical deposition of nanoparticles of noble metals of Ag and Au on NAA increases of the RIfS shift and the sensitivity.

Glucose nanosensor which changes color

The porous nature of the NAA film allow it efficiently absorb the different substances. Figure 3 shows RIfS of the metallized U-NAA-Ni-Ag film in the absence of glucose (solid curve) and with glucose (dashed curve; the concentration is 0.0067 mol/L). In the absence of glucose, spectral maximum is located at 570 nm (see solid curve). In the presence of glucose, spectral maximum is shifted to the long-wave region on 58 nm (see dashed curve). The spectral maximum of the interference peak shifts on one half of phase when glucose is applied to the samples; i.e., when glucose concentration is 0.0067 mol/L, the sensor changes color. The glucose fills porous layer and increases the refractive index of NAA, so the wavelength of the reflection maximum is shifted to the long-wave spectral region. In the present paper, in the minimum test of glucose which is applied to the sample, ~ 10^{-9} g of the studied compound is contained. Thus, the detection method of analyte based on the RIfS of the metallized NAA allows determining nanogram amounts of glucose. This gives the possibility to create the simple medical nanosensors and nanosensors for food analysis.

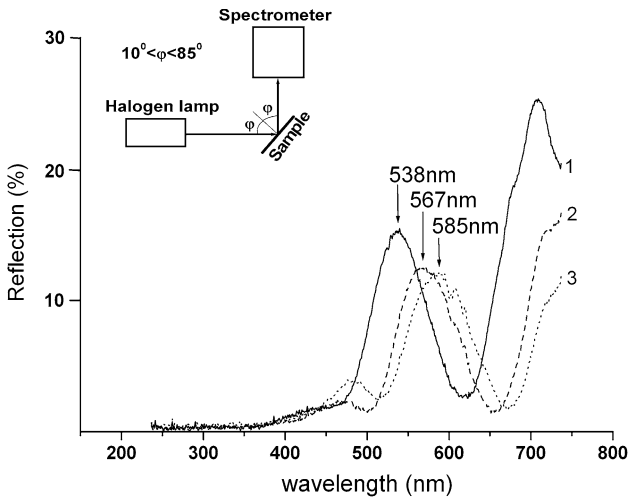

Figure 2 Scheme for measuring of the RIfS and reflection spectra of the metallized NAA film with silver nanoparticles (1) covered by water (2) and ethanol (3) in comparison with aluminum mirror.

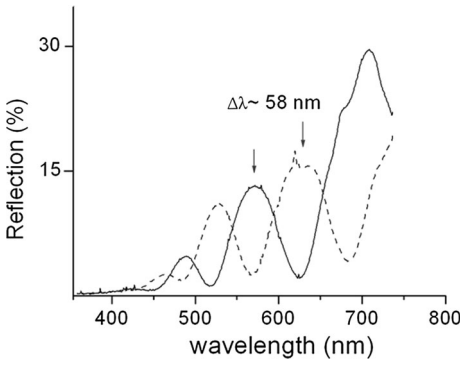

Figure 3 Reflection spectra of porous aluminum oxide film, containing nanoparticles of silver in the absence of glucose (solid curve) and with glucose (dashed curve) in reference to Al mirror. It is seen that the high contrast interference reflection spectrum is shifted one half of phase when glucose is applied to the samples.

Average density of pores and lasers

The electron microscopy image of the A-NAA-Cu-Ag film with average density of pores is shown in Fig. 4. According to electron microscopy studies (see Fig. 4), alumina film has average density of pores. The pore diameter is about 9–15 nm. The pores have a wall thickness from 7 to 10 nm. The porosity is about 21%. As can be seen from Fig. 5, the NAA film has the hexagonal (honeycomb) structure of arrangement of pores. Silver nanoparticles formation after chemical deposition was shown by electron microscopy. The formed silver nanoparticles have a diameter from ≈ 5 to ≈ 85 nm and are located predominantly on the surface (see Fig. 4). During the chemical deposition, silver nanoparticles cover open ends of pores on the surface of the film.

As can be seen from Fig. 4, large silver nanoparticles are distributed on the surface of NAA films at the distance of about 30–250 nm; i.e., the film is not continuous and pores are available for penetration of dye (rhodamine 6G) molecules.

Possible applications are in micro/nanoscale lasers with indirect electrical pumping by laser diodes. NAA films with a high and average density of pores can be used as active medium of lasers. Figure 6 shows the spectrum of laser radiation generation by the film of NAA activated with rhodamine 6G with internal natural nanoresonator. The generation occurs at a wavelength of 572 nm. The line half-width is narrow and amounts to $\Delta\lambda_{FWHM} \approx 10$ nm. It is important to note that a component of spontaneous radiation is completely absent in the induced radiation spectrum. The absence of a spontaneous radiation component indicates the efficient pumping of the energy from the contour of the luminescence spectrum into a line of generation, which, for example, was not achieved in [10]. The transition from the photoluminescence to laser generation by the full absence of a spontaneous component occurs at a value of impinging radiation power density of about $Pw \sim 0.5$ MW/cm^2. By taking into account small sample thickness and low quality of the internal natural nanoresonator, this value can be considered small. Chemical deposition of noble metals leads to a redistribution of nanoparticles from the bottom to the top part of the porous NAA layer. This method

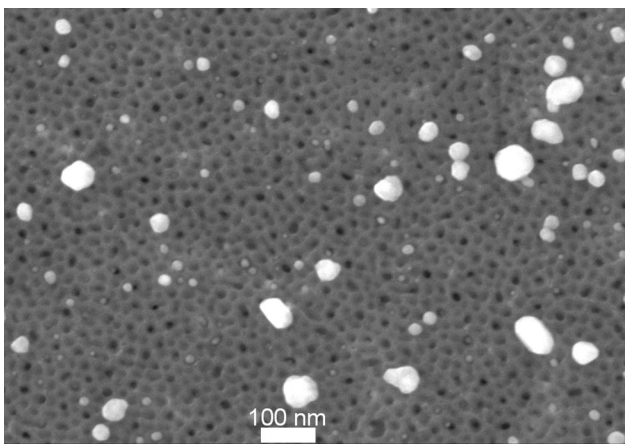

Figure 4 Scanning electron microscopic image of high resolution of metallized nanoporous layer of NAA with silver nanoparticles (top view; average density of pores).

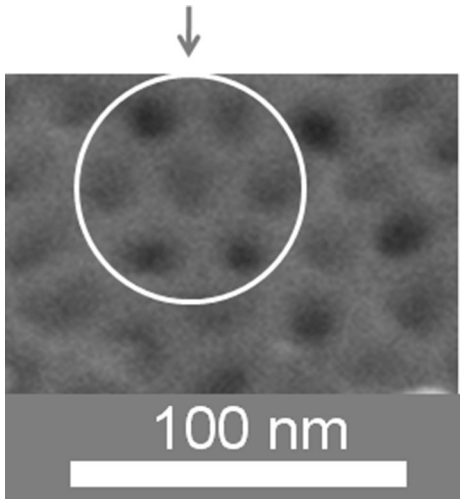

Figure 5 Electron microscopic photograph of superhigh resolution of the film of NAA (top view; hexagonal structure of arrangement of pores).

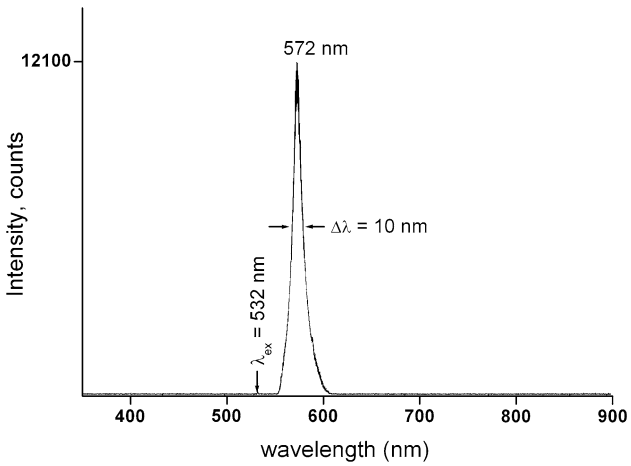

Figure 6 Spectrum of laser radiation generation by the film of NAA. $C_{rhodamine} = 10^{-3}$ mol/L.

achieves a sharper Fabry–Perot interference in a layered structure and reduces generation threshold more than four times.

Low density of pores and the selective interference coloration of the metal surface

Metallized NAA films with low density of pores, a large distance between the pores and thick walls were obtained (see electron microscopic photograph of Fig. 7). The physical and chemical properties of the obtained color NAA films were studied. The porosity is about 7–9%. The RIfS of the alumina films stained by deposition of gold (L-NAA-Cu-Au, dashed curve 4) and silver (L-NAA-Cu-Ag, solid curve 3) nanoparticles in comparison with aluminum mirror are shown in Fig. 7. Just after anodization of the poled aluminum and formation of the oxide layer (L-NAA), the interference color is not visible (dotted curve 1 in Fig. 7). After electrodeposition of the Cu or Ni inside the pores of NAA the interference color appears, depending on the thickness of the initial oxide layer or on the time of the anodic film growth. The reflection spectrum of the aluminum oxide film colored by Cu deposition (L-NAA-Cu), in reference to the Al mirror, is shown in Fig. 7 (curve 2). One can observe the growth of the interference contrast of the reflection peaks. The additional chemical deposition of the noble metal on the cuprum nanoparticles electrodeposited in NAA leads to the noticeable enhancement of the selective reflection ability of the anodized film (see curves 3 and 4). Formation of nanostructures similar to the Fabry–Perot interferometer leads to multiple reflections within the NAA layer, which reinforces the interference contrast of reflection maxima. Table 3 shows values of the interference contrast of the reflection maxima V_i. Interference contrast was calculated using the following formula:

$$V_i = \frac{I_{i\max} - I_{i\min}}{I_{i\max} + I_{i\min}}, \tag{3}$$

where $I_{i\max}$ is the intensity of the corresponding reflection maximum; $I_{i\min}$ is the intensity of the corresponding reflection minimum; i = blank, Cu, Ag, Au, respectively. As can be seen from the table, the interference contrast in the case of a film containing gold nanoparticles is about three times higher than that of a blank film and about two times higher than that of a film with silver nanoparticles. Thus, the chemical enhancement of the interference contrast occurs.

Possible application is selective interference coloration of the metal surface. In addition, the use of the obtained metallized NAA films with low pore density is an effective way to increase the corrosion stability of the metal.

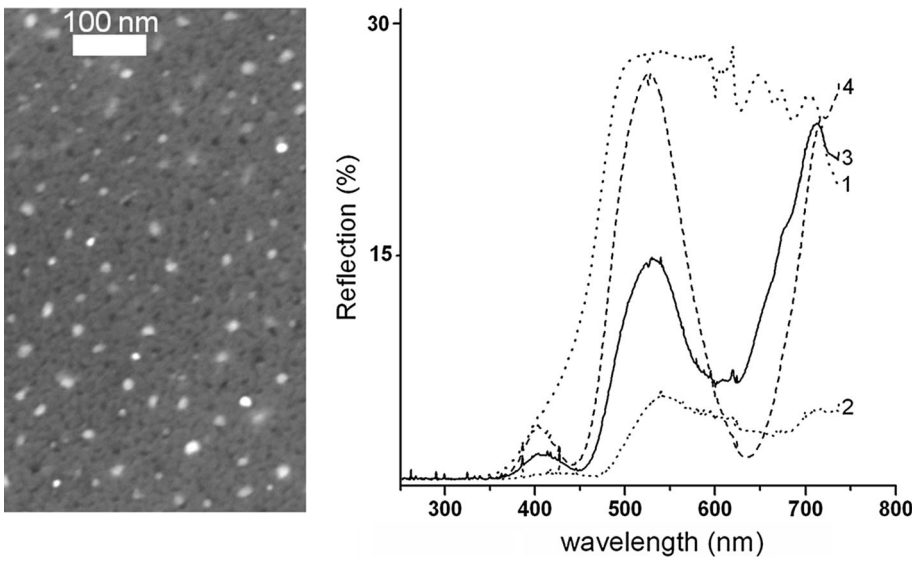

Figure 7 Electron microscopic photograph of superhigh resolution of the metallized film of NAA (top view; low density of pores) and RIfS of colored oxide film with chemical deposited gold (dashed curve 4) and silver (solid curve 3) nanoparticles in reference to Al mirror. The curve (2) is spectrum of the anodized film with Cu. The dotted curve (1) is spectrum of the blank anodized film. It is seen that the difference between the maximum and minimum increases.

Table 3 Values of the interference contrast of the reflection maxima (V_i)

V_i	Value	Curve number in the Fig. 7
V_{blank}	0.01	(1)
V_{Cu}	0.31	(2)
V_{Ag}	0.41	(3)
V_{Au}	0.90	(4)

Polarization anisotropy of reflection spectra and protection of documents

Figure 8 demonstrates the RIfS spectra of P-NAA-Ni film measured for various polarization geometries. The polarization of the light reflected by samples was analyzed in two geometries (*S*-polarized light, line, and *P*-polarized light, dashed line). It is seen that the high contrast interference reflection spectrum is shifted one half of phase when changing the polarization from *S* component to *P* component.

Figure 9 shows the example of polarizing barcode (*S* component, line, and *P* component, dashed line). The degree of polarization $((S - P)/(S + P)) \times 100\%$ for the peak with an energy of 1.77 eV was more than 57%, and that for the peak with an energy of 2.40 eV was more than 50% (see Fig. 9). Possible application is the protection of documents.

Additionally, I should like to note other important applications of samples as catalysts [24] and hyperbolic metamaterials [25–31].

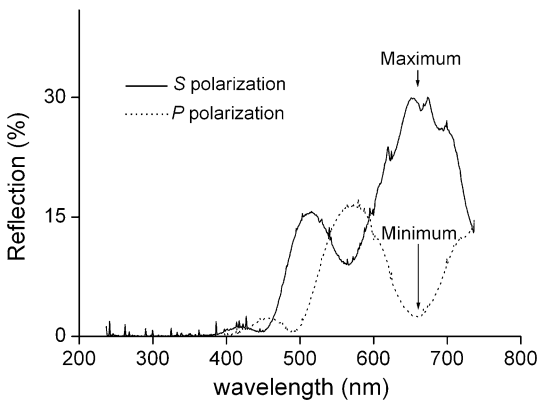

Figure 8 Reflection spectra of the P-NAA-Ni film measured for various polarization geometries (*S*-polarized light, line, and *P*-polarized light, dashed line).

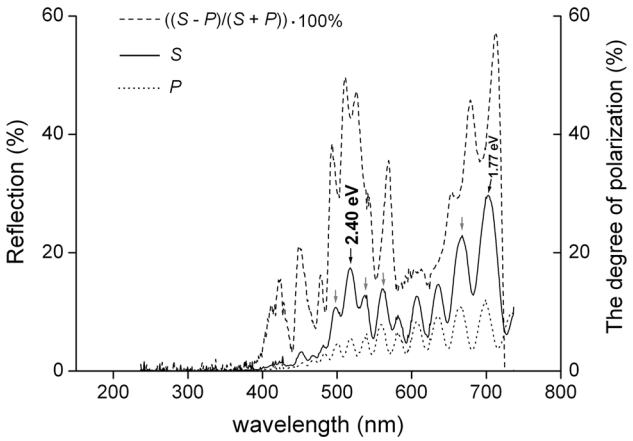

Figure 9 Reflection spectra of the B-NAA-Ni film and the degree of polarization $((S - P)/(S + P)) \times 100\%$.

Conclusion

The nanoporous structures with ultrahigh, average, and low density of pores were obtained using nanoscale electrochemistry. The physical and chemical properties of the obtained metallized nanoporous anodic alumina films were studied by the electron microscopy method and the optical reflection spectra at different angles. The conditions of the aluminum electrochemical anodization and electrochemical and chemical metallization were investigated, and the optimal regimes were determined. The possibility of creating an optical interferometric chemical sensor based on the film of metallized nanoporous anodic alumina was demonstrated. In the absence of an external resonator, the generation by a nanoporous anodic alumina film activated with rhodamine 6G has been obtained for the first time. It was shown that the nanoporous anodic alumina films with ultrahigh, average, and low density of pores can be used in optical interferometric sensors, lasers, and in the selective interference coloration of the metal surface, respectively. Interference coloring of nanoporous anodic alumina films is an effective way to increase the corrosion stability of the metal. These phenomena are important for applications in aerospace industry and manufacturing of chemical nanosensors and micro/nanoscale lasers.

Compliance with ethical standards

Conflict of interest The author declares that there is no conflict of interest.

References

[1] Lyubas GA (2017) Generation of laser radiation by nanostructured solid active elements based on nanoporous aluminum oxide films activated with rhodamine 6G. Nanotechnol Russ 12:276–284

[2] Lyubas GA, Shelkovnikov VV, Korotaev SV (2016) Optical interferometric sensor based on thin layers of nanoporous anodized aluminum containing nanoparticles of noble metals. Nanotechnol Russ 11:29–40

[3] Shelkovnikov VV, Lyubas GA, Korotaev SV (2016) Enhanced reflective interference spectra of nanoporous anodic alumina films by double electrochemical deposition of chemical metal nanoparticles. Prot Met Phys Chem Surf 52:227–231

[4] Kumeria T, Rahman MM, Santos A, Ferré-Borrull J, Marsal LF, Losic D (2014) Structural and optical nanoengineering of nanoporous anodic alumina rugate filters for real-time and label-free biosensing applications. Anal Chem 86:1837–1844

[5] Santos A, Kumeria T, Losic D (2014) Nanoporous anodic alumina: a versatile platform for optical biosensors. Materials 7:4297–4320

[6] Santos A, Kumeria T, Losic D (2013) Optically optimized photoluminescent and interferometric biosensors base on nanoporous anodic alumina: a comparison. Anal Chem 85:7904–7911

[7] Ferré-Borrull J, Rahman MM, Pallares J, Marsal LF (2014) Tuning nanoporous anodic alumina distributed-Bragg reflectors with the number of anodization cycles and the anodization temperature. Nanoscale Res Lett 9:416–422

[8] Ferré-Borrull J, Pallares J, Macias G, Marsal LF (2014) Nanostructural engineering of nanoporous anodic alumina for biosensing applications. Materials 7:5225–5253

[9] Macias G, Hernández-Eguía LP, Ferré-Borrull J, Pallares J, Marsal LF (2013) Gold-coated ordered nanoporous anodic alumina bilayers for future label-free interferometric biosensors. ACS Appl Mater Interfaces 5:8093–8098

[10] Marinho SJ, Jesus LM, Barbosa LB, Ardila DR, Alencar M, Rodrigues JJ Jr (2015) Bi-chromatic random laser from alumina porous ceramic infiltrated with rhodamine B. Laser Phys Lett 12:055801–055805

[11] Zhang W, Yao J, Zhao YS (2016) Organic micro/nanoscale lasers. Acc Chem Res 49:1691–1700

[12] Li YJ, Yan Y, Zhao YS, Yao J (2016) Construction of nanowire heterojunctions: photonic function-oriented nanoarchitectonics. Adv Mater 28:1319–1326

[13] Zhang ZL, Zheng HR, Dong J, Yan XQ, Sun Y, Xu HX (2012) Surface enhanced fluorescence by porous alumina with nanohole arrays. Sci China Ser G 55:767–771

[14] Moon JM, Wei A (2005) Uniform gold nanorod arrays from polyethyleniminecoated alumina templates. J Phys Chem B 109:23336–23341

[15] Nielsch K, Muller F, Li AP, Gosele U (2000) Uniform nickel deposition into ordered alumina pores by pulsed electrodeposition. Adv Mater 12:582–586

[16] Belov A, Gavrilov S, Shevyakov V, Redichev E (2011) Pulsed electrodeposition of metals into porous anodic alumina. Appl Phys A Mater Sci Process 102:219–223

[17] Hwang SK, Jeong SH, Lee OJ, Lee KH (2005) Fabrication of vacuum tube arrays with a submicron dimension using anodic aluminum oxide nanotemplates. Microelectron Eng 77:2–7

[18] Ng CKY, Ngan AHW (2011) Precise control of nanohoneycomb ordering over anodic aluminum oxide of square centimeter areas. Chem Mater 23:5264–5268

[19] Guo Y, Zhou L, Kameyama H (2011) Thermal and hydrothermal stability of a metal monolithic anodic alumina support for steam reforming of methane. Chem Eng J 168:341–345

[20] Alam KM, Singh AP, Bodepudi SC, Pramanik S (2011) Fabrication of hexagonally ordered nanopores in anodic alumina: an alternative pretreatment. Surf Sci 605:441–449

[21] Devan RS, Patil RA, Lin JH, Ma YR (2012) Onedimensional metaloxide nanostructures: recent developments in synthesis, characterization, and applications. Adv Funct Mater 22:3326–3370

[22] Zhang D, Zhang H, He Y (2006) In situ thickness measurement of porous alumina by atomic force microscopy and the reflectance wavelength measurement from 400–1000 nm. Microsc Res Tech 69:267–270

[23] Chen CY, Huang JH, Song JH, Zhou YS, Lin L, Huang PC, Zhang Y, Liu CP, He JH, Wang ZL (2011) Anisotropic outputs of a nanogenerator from oblique-aligned ZnO nanowire arrays. ACS Nano 5:6707–6713

[24] Sadykov V, Parmon V, Tikhov S (2009) Design of some oxide/metal composite supports and catalysts. Compos Interfaces 16:457–476

[25] Ginzburg P, Rodriguez-Fortuno FJ, Wurtz GA, Dickson W, Murphy AP, Morgan F, Pollard RJ, Iorsh IV, Atrashchenko AV, Belov PA, Kivshar YS, Nevet A, Ankonina G, Orenstein M, Zayats AV (2013) Manipulating polarization of light with ultrathin epsilon-near-zero metamaterials. Opt Express 21:14907–14917

[26] Simovski CR, Belov PA, Atrashchenko AV, Kivshar YS (2012) Wire metamaterials: physics and applications. Adv Mater 24:4229–4248

[27] Barnakov YA, Kiriy N, Black P, Li H, Yakim AV, Gu L, Mayy M, Narimanov EE, Noginov MA (2011) Toward

curvilinear metamaterials based on silver-filled alumina templates. Opt Mater Express 1:1061–1064

[28] Naik GV, Kim J, Boltasseva A (2011) Oxides and nitrides as alternative plasmonic materials in the optical range. Opt Mater Express 1:1090–1099

[29] Noginov MA, Barnakov YuA, Li H, Zhu G, Tumkur TU, Mayy M, Jacob Z, Alekseyev L, Narimanov EE (2010) Silver-filled alumina membrane: metamaterial with hyperbolic dispersion and near-zero singularity. Photonic metamaterials and plasmonics, p MTuA4

[30] Noginov MA, Barnakov YA, Zhu G, Tumkur T, Li H, Narimanov EE (2009) Bulk photonic metamaterial with hyperbolic dispersion. Appl Phys Lett 94:151105–151110

[31] Yao J, Liu Z, Liu Y, Wang Y, Sun C, Bartal G, Stacy AM, Zhang X (2008) Optical negative refraction in bulk metamaterials of nanowires. Science 321:930

[32] Gerrard EJP, Nurshahidah A, Derek F (2011) Progress in nano-engineered anodic aluminum oxide membrane development. Materials 4:487–526

[33] Ebihara K, Takahashi H, Nagayama M (1983) Structure and density of anodic oxide films formed on aluminum in oxalic acid solutions. J Met Finish Soc Jpn 34:548–553

[34] Anker JN, Hall WP, Lyandres O, Shah NC, Zhao J, van Duyne RP (2008) Biosensing with plasmonic nanosensors. Nat Mater 7:442–453